

Validation of Under-Resolved Numerical Simulations of the PDC Exhaust Flow Based on High Speed Schlieren



M. Nadolski, M. Rezay Haghdoost, J. A. T. Gray, D. Edgington-Mitchell, K. Oberleithner and R. Klein

Abstract Owing to their high thermodynamic efficiency, pulsating combustion cycles have become an attractive option for future gas turbine designs. Yet, their potential gains should not be outweighed by losses due to unsteady pressure wave interactions between engine components. Consequently, the geometric engine design moves into focus. Ideally, one would quickly test several different principal layouts with respect to their qualitative behavior, select the most promising variants and then move on to detailed optimization. Computational fluid dynamics (CFD) appears as the methodology of choice for such preparatory testing. Yet, the inevitable geometric complexity of such engines makes fully resolved CFD an arduous and expensive task necessitating computations on top high-performance hardware, even with modern adaptive mesh refinement in place. In the present work we look at the initial flow field of a shock generated by a pulse detonation combustor (PDC) which leaves the combustion chamber and enters the plenum. We provide first indicators, however, that overall mechanical loads, represented by large-scale means of, e.g., mass, energy, and momentum fluxes can be well estimated on the basis of rather coarsely resolved CFD calculations. Comparing high-resolution simulations of the exit of a strong shock from a combustion tube with experimental schlieren photographs, we first

M. Nadolski (✉) · R. Klein
Freie Universität Berlin, Berlin, Germany
e-mail: nadolski@math.fu-berlin.de

R. Klein
e-mail: rupert.klein@math.fu-berlin.de

M. R. Haghdoost · J. A. T. Gray · K. Oberleithner
Technische Universität Berlin, Berlin, Germany
e-mail: mohammad.rezayhaghdoost@campus.tu-berlin.de

J. A. T. Gray
e-mail: joshua.gray@tu-berlin.de

K. Oberleithner
e-mail: oberleithner@tu-berlin.de

D. Edgington-Mitchell
Monash University, Melbourne, VIC, Australia
e-mail: daniel.m.mitchell@gmail.com

establish validity of fully resolved CFD. Next we compare several integral quantities representative of overall mechanical loads with a sequence of successively coarser grid simulations, thereby corroborating that the “quick and dirty” coarse-grained simulations indeed allow for good order of magnitude estimates.

Keywords Coarse resolution CFD code validation
Experimental Schlieren visualization · Expansion from detonation tube

1 Introduction

Pulsating combustion cycles of varying design are currently being discussed as a way to approximately achieve constant volume combustion (CVC) in gas turbines. Approximate CVC (aCVC) is desirable due to its considerably higher thermodynamic efficiency in comparison with the standard deflagrative combustion which progresses at approximately constant pressure. To accommodate pulsating combustion in a gas turbine, unsteady gasdynamic effects have to be carefully controlled to avoid excessive mechanical and thermal loads and, depending on the nature of the combustion cycle, to optimize its efficiency and robustness. Nonstationary compressible flow in enclosed domains depends crucially on the domain geometry, and we conclude that the design process for a new class of gas turbines involving pulsating aCVC requires flexible geometric design capabilities.

Support comes from modern Computational Fluid Dynamics (CFD) techniques and codes which allow the user to simulate flows in rather complex geometries utilizing, e.g., Cartesian grid cut cell methods [2, 3, 6–9]. Despite the general geometrical flexibility provided by these techniques, three-dimensional fully resolved simulations in complex geometries are highly demanding, and can hardly be used routinely for quick estimates of the principal consequences of major design alternatives. A central hypothesis of the present project (see the conclusions) is that the overall mechanical and thermal loads on enclosure confinements do not depend on the fine-scale structure of gasdynamic processes, but rather on their coarse-grained averaged behavior. If this hypothesis can be corroborated, then an efficient hierarchical approach to the geometrical design of pulsating combustion gas turbines may be adopted: One would first pursue a quick scan of various major geometrical design options utilizing coarse-resolution numerical approximations that can be run in tens of minutes on a PC, and only turn to high-resolution expensive super-computer-based simulations with excessive detail when the overall design has been fixed. To make such an approach feasible, however, we must first validate our base hypothesis and the present study represents a first step in this direction. This task is approached here through the following steps:

1. A laboratory experiment that involves strong multi-dimensional gasdynamic effects is reproduced by highly resolved numerical simulations.

2. A sequence of simulations with successively coarser resolution follows, the coarsest chosen such that all small-scale detail is smeared out by the finite volume averaging of the conservative numerical scheme.
3. Finally, several integral quantities, such as mean mass and momentum fluxes across some pre-defined large-scale surfaces, is monitored and compared between the members of the ensemble of coarser and coarser simulation runs.

These steps will provide estimates of how coarse a resolution, i.e., how efficient a computation, can be afforded to still obtain good quantitative or at least qualitative insights into the large-scale features of a highly unsteady flow.

In the present first test we consider experimental schlieren photographs of a strong shock wave exiting a cylindrical tube. The shock has been generated within a tube partially filled with a combustible mixture by firing a deflagration from its left end into an accelerator section. The ensuing high-speed turbulent flame generates a strong shock which then meets the inert column of air that covers the remainder of the tube. Figure 4 shows the geometrical setup and Fig. 5, left panel, shows the situation immediately after the shock has exited the tube (see also Sect. 4 for experimental details). We see the leading shock still being essentially plane near the axis of symmetry, but bending outwards where it expands into the surrounding air.

We follow the evolution of this flow over the first few hundred micro seconds and compare idealized two-dimensional axisymmetric and three-dimensional cartesian numerical simulations for this case in Sect. 6. That section also shows the comparison of some integral quantities computed for a high-resolution reference simulation and a sequence of *coarser* runs to demonstrate that such overall estimates can well be computed based on very rough, crudely resolved simulations. Before we get to this, however, we first describe the mathematical formulation of the flow problem in Sect. 2, the numerical method and code used in Sect. 3, and the specific numerical setup of the simulation runs in Sect. 5. Section 7 draws conclusions and provides future perspectives.

2 Governing Equations

2.1 Summary of the Equations in Cartesian Coordinates

We consider the homogeneous Euler equations in conservative form, i.e.,

$$\frac{\partial}{\partial t} \rho + \nabla \cdot (\rho \mathbf{V}) = 0 \quad (\text{Conservation of Mass}) \quad (1)$$

$$\frac{\partial}{\partial t} (\rho \mathbf{V}) + \nabla \cdot [\rho \mathbf{V} \otimes \mathbf{V} + p \mathbb{I}] = 0 \quad (\text{Conservation of Momentum}) \quad (2)$$

$$\frac{\partial}{\partial t} (\rho E) + \nabla \cdot [(\rho E + p) \mathbf{V}] = 0 \quad (\text{Conservation of Total Energy}) \quad (3)$$

where ρ , p , E and $\mathbf{V} = (u, v, w)$ are density, pressure, total energy, and the velocity vector respectively, \otimes denotes the tensor product, and \mathbb{I} the identity matrix. To close the system we choose the equations of state for perfect gases

$$p = \rho(\gamma - 1) \left(E - \frac{\mathbf{V}^2}{2} \right). \quad (4)$$

Here γ is the ratio of specific heat capacities, $\gamma = c_p/c_v$, and is set to a value of $\gamma = 1.4$ throughout this study. Equations (1)–(3) can also be written in a form useful when applying dimensional splitting as in the present study,

$$\mathbf{U}_t + \mathbf{F}(\mathbf{U})_x + \mathbf{G}(\mathbf{U})_y + \mathbf{H}(\mathbf{U})_z = 0 \quad (5)$$

with

$$(\mathbf{U}, \mathbf{F}, \mathbf{G}, \mathbf{H}) = \left(\begin{pmatrix} \rho \\ \rho u \\ \rho v \\ \rho w \\ \rho E \end{pmatrix}, \begin{pmatrix} \rho u \\ \rho u^2 + p \\ \rho uv \\ \rho uw \\ \rho Hu \end{pmatrix}, \begin{pmatrix} \rho v \\ \rho uv \\ \rho v^2 + p \\ \rho vw \\ \rho Hv \end{pmatrix}, \begin{pmatrix} \rho w \\ \rho uw \\ \rho vw \\ \rho w^2 + p \\ \rho Hw \end{pmatrix} \right) \quad (6)$$

and the total specific enthalpy $H = E + p/\rho$.

2.2 Axi-Symmetric Flows

For axisymmetric arrangements, (1)–(3) are conveniently recast in terms of cylindrical coordinates. Let the x -axis represent the axis of symmetry, then (5) transforms to, [12],

$$\mathbf{U}_t + \mathbf{F}(\mathbf{U})_r + \mathbf{G}(\mathbf{U})_x = \mathbf{S}(\mathbf{U}), \quad (7)$$

with

$$(\mathbf{U}, \mathbf{F}, \mathbf{G}, \mathbf{S}) = \left(\begin{pmatrix} \rho \\ \rho u \\ \rho v \\ \rho E \end{pmatrix}, \begin{pmatrix} \rho u \\ \rho u^2 + p \\ \rho uv \\ \rho Hu \end{pmatrix}, \begin{pmatrix} \rho v \\ \rho uv \\ \rho v^2 + p \\ \rho Hv \end{pmatrix}, -\frac{1}{r} \begin{pmatrix} \rho u \\ \rho u^2 \\ \rho uv \\ \rho Hu \end{pmatrix} \right). \quad (8)$$

Here u is now the radial and v the velocity along the x axis.

3 Numerical Methods

Pulsating combustion cycles for near stoichiometric hydrocarbon-air or hydrogen-air mixtures come with pressure wave amplitude ratios of p/p_{ref} ranging from 4 to 20, depending on the combustion mode. Thus, strong shocks ensue and we have no alternative but to use conservative numerical schemes to solve the Euler equations. In this study we use the MUSCL-Hancock, [13], conservative finite volume method. This scheme is second order accurate and employs slope-limiting near discontinuities to prevent the formation of spurious oscillations. The scheme is conveniently employed for multiple space dimensions using Strang splitting [11]. For the representation of complex geometries, we use a cut-cell technique [8]. To evolve the source term in (7) we use again Strang splitting, advancing the solution in the related split step by an adaptive Runge-Kutta-45 scheme.

The code, which is a joint development with the Centre for Scientific Computing, Cavendish Laboratory, Cambridge University, is capable of using block structured adaptive mesh refinement (AMR) similar to [1]. This capability is not utilized in the present study, however, as we intend to first understand the basic behavior of this numerical methodology under grid coarsening.

4 Experiment: Strong Shock Exiting a Straight Tube

In order to generate a shock wave propagating through a tube, a pulse detonation combustor (PDC) is used in this study. The schematic of the PDC and the instrumentation of the experimental setup is shown in Fig. 1. The PDC consists of two sections: the section in which the flame acceleration and subsequent deflagration-to-detonation transition (DDT) occurs and the exhaust tube. Hydrogen and air are injected into the upstream end of the tube. Combustion is initiated with a spark plug, positioned at the upstream end of the DDT section. The specific design of the hydrogen and air injection schemes is described in [5].

Once the mixture is ignited, orifices positioned in the DDT section accelerate the flame propagation. The speed of the leading shock wave is determined by five piezoelectric pressure sensors (PCB112A05), flush-mounted in the exhaust tube, as shown in Fig. 1. In order to assess whether the transition from deflagration to detonation takes place before entering the exhaust tube, three additional closely spaced pressure probes are placed in the downstream end of the DDT section.

The reaction front is tracked inside the tube by three flush-mounted ionization probes on the opposite side from the pressure sensors. The ionization probes, fabricated in-house, consist of two electrodes separated by a ceramic coating. When a potential difference is applied to the electrodes, the ionized species in the combustion region allow for an electric current to flow. The resulting voltage drop marks the arrival of the combustion front.

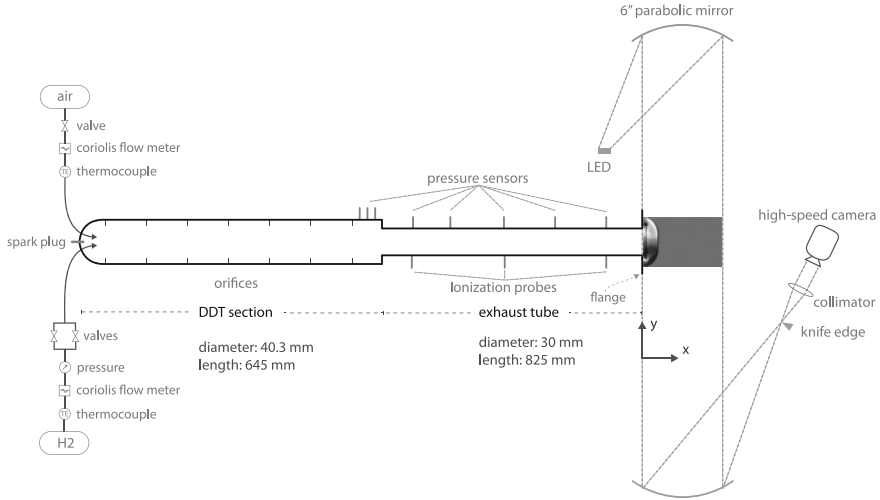


Fig. 1 Sketch of the experimental setup showing the pulse detonation combustor, pressure sensors and ionization probes for reaction front and pressure wave detection, and the high-speed schlieren setup at the tube exit

Data is acquired simultaneously on 11 channels using a National Instruments MXI-Express DAQ system at a sampling rate of 1 MHz. The mass flow rate of air and hydrogen is measured with Endress + Hauser Coriolis mass flow meters. Two type K thermocouples are used to measure the temperature of air and hydrogen. The pressure of the hydrogen fuel line upstream of the injection valves is measured with a Festo pressure transmitter (SPTW-P10R).

The high-speed schlieren images are acquired with a Photron SA-Z high-speed camera at frequencies up to 80 kHz. A standard z-type schlieren configuration is used with two 6-inch parabolic $f/8$ mirrors for collimating and refocusing of light. As a light source, a pulsed LED is used as suggested by Willert et al. [14]. The overdriven-operated LED provides a light pulse with very high intensity at very short time span ($1 \mu\text{s}$).

The operating condition of the PDC can be adjusted to maintain high conformity with the numerical simulations. Since the numerical models do not account for chemical reactions, it is desirable to minimize the impact of combustion on the flow evolution once the shock wave exits the tube. Therefore, the PDC is filled only partially with combustible mixture to allow for the shock wave to decouple from the reaction front and maintain a time gap between the shock wave and combustion products leaving the tube.

The shock wave velocity along the PDC is shown in Fig. 2. The wave velocity is captured at seven axial positions via eight pressure probes. The shock wave velocity of 1000 m/s within the DDT section is about half the Chapman-Jouguet (CJ) velocity. Because the tube is only partially filled, the deflagration wave does not transition to a detonation wave. The shock wave is transmitted to the air, while the reaction

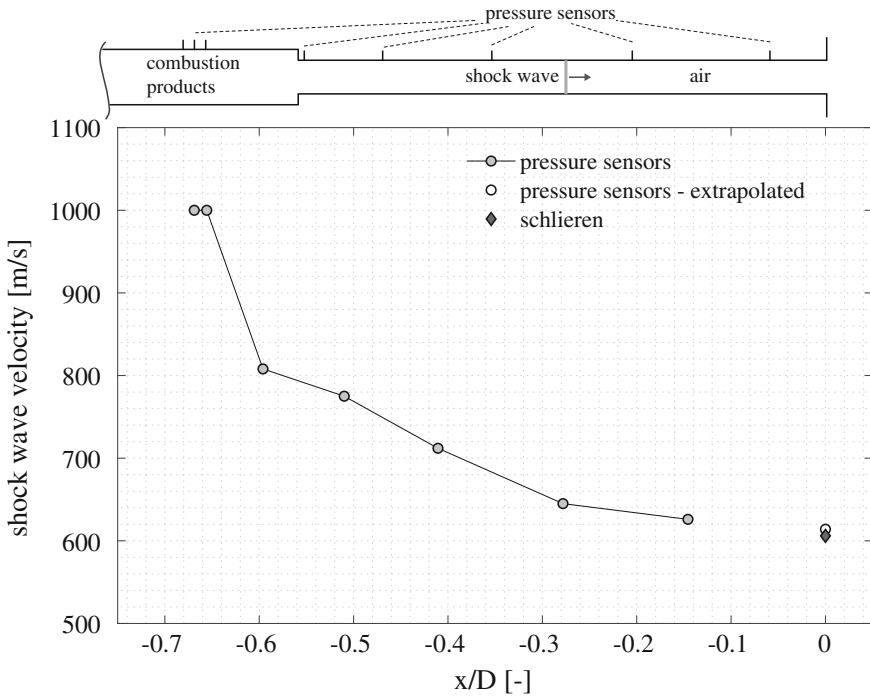


Fig. 2 Leading shock wave velocity determined by the pressure sensors in the tube and three consecutive schlieren images at the tube outlet

front is extinguished as the deflagration wave reaches the intersection of the reactive mixture with air. The decelerating shock wave propagates through the exhaust tube while compressing the air. The shock wave diffracts through the atmosphere once it reaches the tube exit. The flow evolution at the tube exit is captured by means of schlieren images. These images are used for validation of the numerical simulations.

The primary parameter that sets the initial condition for the numerical simulation is the shock wave Mach number at the exit of the tube. Hence, the shock wave velocity has been determined via two independent methods using schlieren images and pressure probes. Therefore, consecutive schlieren images captured at 80 kHz are used as shown in Fig. 3. The straight vertical shape of the leading shock in all three frames indicates that the information about the area expansion at the tube outlet has not yet reached the jet centerline. This implies that the shock velocity is still the same as directly after the tube exit without any deceleration due to shock wave diffraction [10]. Consequently the shock velocity and related Mach number can be unambiguously determined from the shock displacement shown in Fig. 3, using the time-of-flight. The determined shock wave velocity of 606 m/s corresponds to an exit Mach number of $M = 1.77$. The exit velocity of the shock wave at the tube exit can also be estimated from the pressure sensor signals. Therefore, the arrival time of the

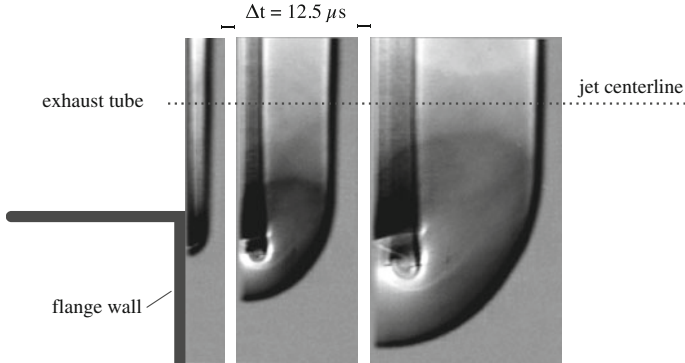


Fig. 3 Three consecutive schlieren images for determining the shock velocity at the exit of the tube

shock wave is extrapolated based on piecewise cubic hermite polynomials (PCHIP) [4] to the tube exit from the arrival times measured at six different streamwise locations. As shown in Fig. 2, the shock velocity determined from schlieren images and the one extrapolated from the pressure signals are in very good agreement with a discrepancy of 1.3%. For this reason, the experimental schlieren images can be used as a benchmark for validation of computational simulations.

5 The Numerical Setup

The geometry of the problem is given as a linear, cylindrical tube leading into a theoretically infinite half space filled with air at room temperature. Figure 4 displays the computational domain of our three-dimensional computation as well as the simplified configuration for the axisymmetric case.

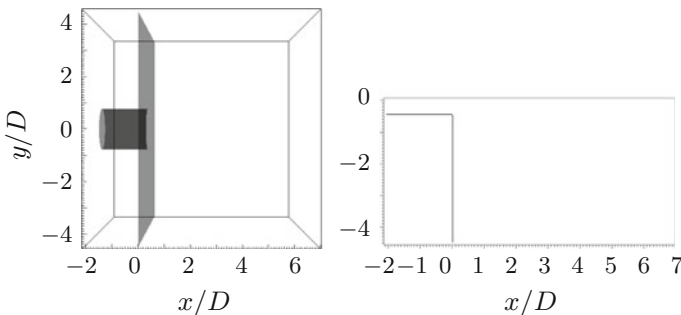


Fig. 4 Left: the computational domain for the three dimensional case, Right: the computational domain for the two dimensional case in cylindrical coordinates

For a simple approximation to the experiment described in Sect. 4 we estimated the velocity of the leading shock from measured data as described in the previous section. The estimate used here is $u_S \approx 585 \frac{m}{s}$, equivalent to a Mach number of $M_S \approx 1.72$, and within a 3% window around the estimate given above. Thus, the simulation begins with an ideal one-dimensional shock of this strength traveling downstream the tube. The upstream boundary conditions in the tube are set to match the post-shock conditions, indicated by a * subscript below. These result from a given state U_{Air} ahead of the shock and from the shock Mach number M_S via the Rankine-Hugoniot conditions reading

$$\frac{\rho_*}{\rho_{Air}} = \frac{(\gamma + 1)(M_{Air} - M_S)^2}{(\gamma - 1)(M_{Air} - M_S)^2 + 2} \quad (9)$$

$$\frac{p_*}{p_{Air}} = \frac{2\gamma(M_{Air} - M_S)^2 - (\gamma - 1)}{(\gamma + 1)} \quad (10)$$

$$u_* = u_S \left(1 - \frac{\rho_{Air}}{\rho_*} \right) + u_{Air} \frac{\rho_{Air}}{\rho_*} \quad (11)$$

Assuming $\gamma = 1.4$, $p_{Air} = 1.01 \cdot 10^5$ Pa, $\rho_{Air} = 1.22$ kg/m³ and $u_{Air} = 0$ m/s we obtain the post-shock state $p_* = 3.33 \cdot 10^5$ Pa, $\rho_* = 2.73$ kg/m³ and $u_* = 323$ m/s.

The computational domain is necessarily limited. To match the experimental setup we have to utilize approximate non-reflecting boundary conditions on all domain boundaries intersecting with the open half space into which the shock wave is expanding. We have adopted a simple version of such a numerical condition. A two cell wide layer of ghost cells surrounds the computational domain. At the beginning of each time step, these cells are assigned the same states found in their next neighbor cells within the computational domain in the sense of a zeroth order extrapolation. This procedure is simple and rather effective, although some weak wave reflection is seen when the shock hits the outer boundaries. For the targeted coarse-grained estimates of integral loads, such a straightforward boundary condition formulation seems appropriate.

To validate our code we set up multiple sets of numerical computations, one for each of the coordinate systems described above and several three dimensional computations in varying resolution. To compare the computations to each other we set the finest grid resolution to 512 cells in each direction, corresponding to cell sizes of $6 \cdot 10^{-4}$ m, and simulate the first two milliseconds. For the three dimensional simulation in Cartesian coordinates this implies $512^3 = 134.217.728$ cells and $256 \cdot 512 = 131.072$ cells for the simulation in cylindrical coordinates. Experimental observations are then compared with these reference runs, while we compare several integral quantities indicative of mechanical loads between these highest resolution and other simulations based on coarser grids below.

6 Results

6.1 Comparison of High-Resolution Runs with the Experiment

Schlieren pictures from the experiment are available in intervals of 50 ms. For the subsequent discussion we set the clock to time $t = 0$ at the instance shown in Fig. 5, when the shock has just exited the tube. Simulation data are available for each consecutive 50 ms after this point in time.

Figure 6 compares experimental data with path integrated schlieren images post-processed from the simulation data of the three-dimensional simulation. To be precise, the figure displays grey scales of the quantity

$$S(x, y) = \int_{z_0}^{z_1} \frac{\partial \rho}{\partial y}(x, y, z) dz. \quad (12)$$

The comparison in Fig. 6 shows that the early evolution is successfully captured in terms of key flow features such as the vortex position, the Mach disk, the reflected shocks, and the slip lines.

On the downside we also observe a mismatch in the position and width of the Mach disk, which increases with time. This discrepancy is likely due to the simplified computational set-up which assumes a shock travelling at constant velocity to exit from the tube. In the experiment, in contrast, the observed shock was generated by firing a high-speed deflagration in the tube and letting the generated strong shock pass over a buffer region of inert gas covering roughly the latter third of the tube length. A strong indication that the upstream conditions between experiment and simulation do not match well after some time is the exit of multiple shocks from the tube seen in the third panel on the left in Fig. 6. This feature is absent from the numerical simulation, because of the exact match of the post-shock conditions of the initial shock at the upstream end of the short tube section included in the simulation. A more realistic set-up that utilizes a one-dimensional version of the compressible

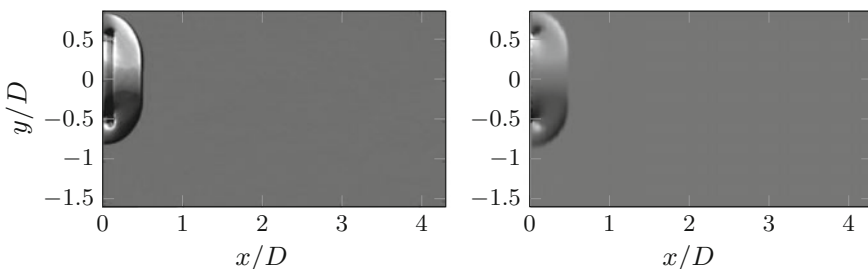


Fig. 5 Experimental schlieren versus path-integrated schlieren from numerical simulations at the reference time $t = 0$

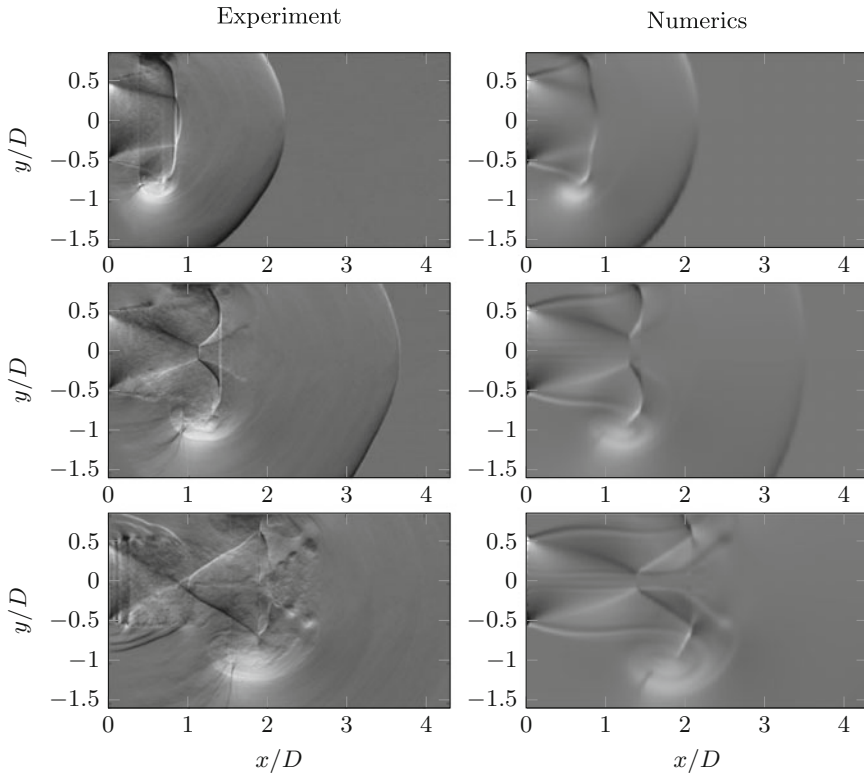


Fig. 6 Comparison with the experiment: path integrated schlieren pictures, at relative time points 100, 200 and 300 μs

(reactive) flow solver to also represent this non-trivial gasdynamic process in the tube prior to the shock wave exit is work in progress.

Nevertheless, the simulation up to time point 100 μs shows results which are close to the experiment. At later times all major flow features are qualitatively present. The quantitative disagreement may be hampered by overly simplified inflow boundary conditions in the numerical simulations.

6.2 Comparison of Different Coordinate Systems

We are interested in the differences between the computations with respect to the two different coordinate systems introduced in Sect. 2. From now on we consider planar density gradients $P(x, y) = |\nabla\rho(x, y, 0)|$, since these reveal more details of the flow. Figure 7 shows that the computation in cylindrical coordinates is in good

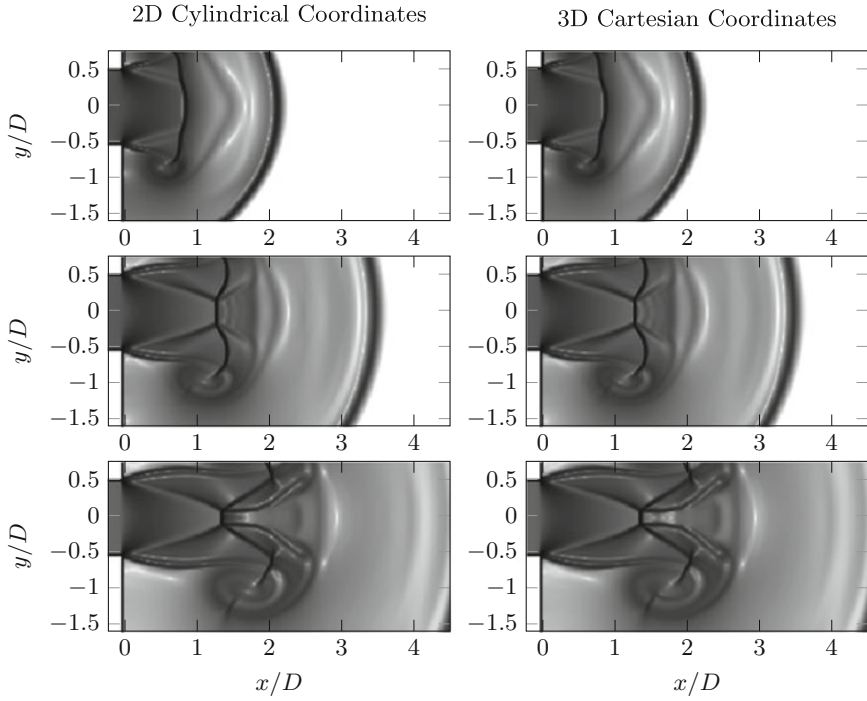


Fig. 7 Comparison of density gradients at relative time points 100, 200 and 300 μ s

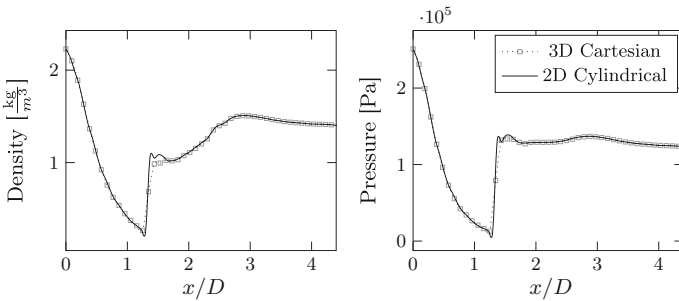


Fig. 8 Plots for density (left) and pressure (right) in $y = z = 0$ over the x position for the relative time point 300 μ s

agreement with the three dimensional computation. Only beyond the relative time point of 300 μ s a sizeable difference is seen in the region around the Mach disk.

Figure 8 displays the pressure and density distribution along the central axis in the flow direction. Good quantitative match between the simulations is obtained. As in the visualisation for the density gradients we see differences in the Mach disk area.

6.3 Effects of Resolution

As stated earlier, we are interested in utilizing quick coarse-resolution simulations for efficient testing of different engine geometries with respect to their influence on overall mechanical loads. Thus, in this section we test whether some globally integrated quantities can well be estimated from such coarse simulations.

Figure 9 illustrates the solution structure for varying resolutions. With a tube diameter of 0.03 m and a resolution of approximately $\Delta x \approx 0.0046$ m the coarsest simulation uses around 6 cells in each direction to cover the tube inlet. Despite being shifted basic structural properties such as shocks, Mach disk and vortex positions are still represented down to the resolution of 128 cells per dimension.

Figure 10 displays the time series of averaged radial mass flow

$$\dot{m}_{rad} = \int_S \rho \mathbf{V} \cdot \mathbf{n}_S dS \tag{13}$$

for these resolutions, where S is the prolongation of the tube wall beyond the tube exit. In analogy with the radial mass flow we also show the axial mass flow integrated over a plane vertical to the tube axis and placed at $x/D = 1.7$ downstream the tube exit.

Figures 11 and 12 show the amount of advected radial and axial momentum through these surfaces,

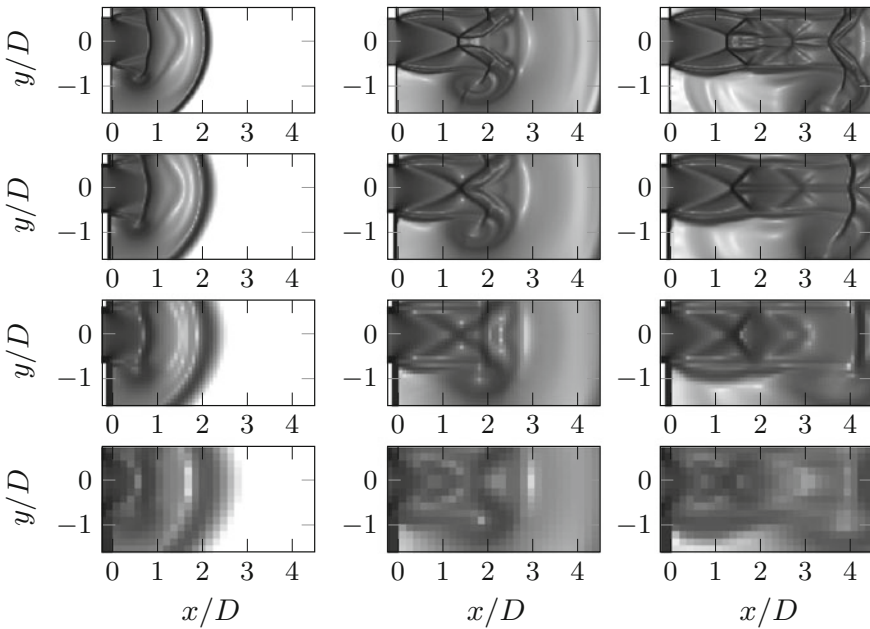


Fig. 9 Comparison of density gradients for a simulation with 512, 256, 128 and 64 cells per dimension at relative time points 100, 300 and 600 μ s

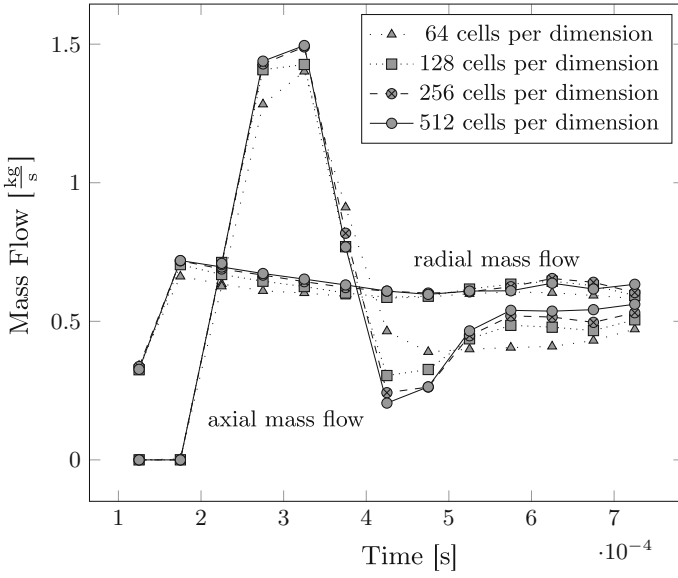


Fig. 10 Radial and axial massflow over time

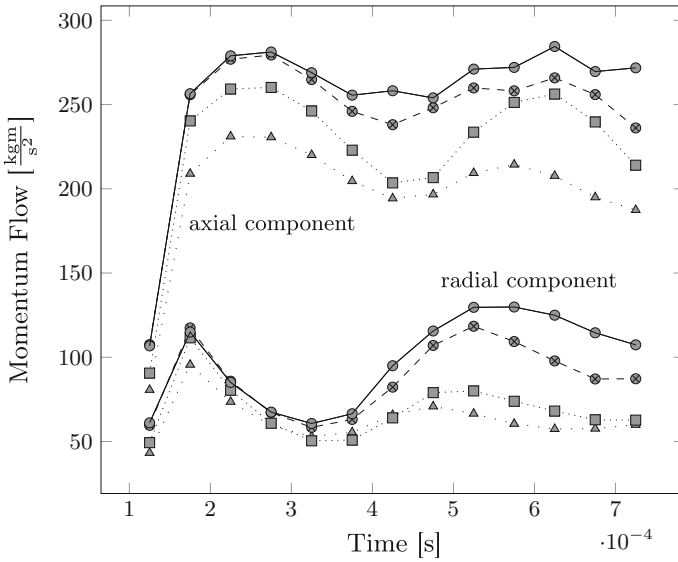


Fig. 11 Radial momentum flow over time

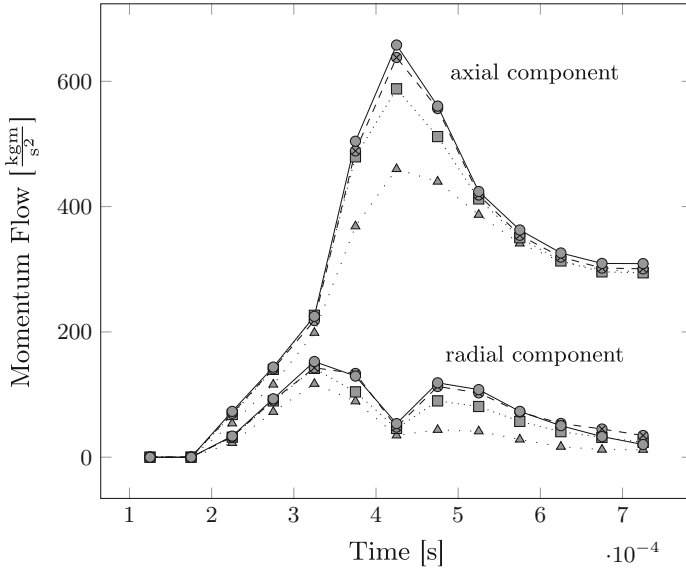


Fig. 12 Axial momentum flow over time

$$\dot{P}_A = \int_A \rho V(V \cdot n_A) dA, \tag{14}$$

where A is the prolonged tube or the vertical plane respectively. Note that while mass flow is a scalar, the momentum flow is a vector which we separated into its axial and radial components and in this study the axial component is equal to the projection onto the axis along the tube, the x -axis. For the radial component of the momentum flow we visualise the magnitude of its y and z components, i.e. let \dot{P}_A be written as $\dot{P}_A = (p_A, q_A, r_A)$, then the axial component of the momentum flow is

$$\text{axial } \dot{P}_A = p_A$$

and its radial component is

$$\text{radial } \dot{P}_A = \sqrt{q_A^2 + r_A^2}.$$

Figures 10 and 12 show good qualitative agreement across all resolutions but the coarsest resolution with 64 cells. Whereas we observe larger discrepancies in Fig. 11, where coarser simulations tend to underestimate the radially advected momentum. Comparing the outgoing stream throughout the computations, we also observe that it is substantially more smeared out for coarse grids. By choosing a relatively narrow cylindrical surface to compute the radial flows, we introduce additional numerical errors while interpolating values on that surface. This might result in not “seeing”

the radial momentum for coarse computations for this particular choice and could be mitigated by choosing a larger radius for the radial test surface.

7 Conclusion

We used a simple and reproducible test case and experiments with numerical simulations. Despite the assumed simplified initial and boundary conditions the simulations resolve the dynamics of a shock exiting a combustion tube. An axisymmetric computational model produces essentially the same results as a full 3D code. We conclude that three-dimensional effects of turbulence are not relevant throughout this early stage. Coarse resolution runs reproduce large-scale averaged quantities potentially important for overall loads quite well in comparison with highly resolved computations. In fact, even key solution features are maintained qualitatively as well as quantitatively. This encourages the use of under-resolved simulations for efficient design studies of engine geometries. Subsequent studies will focus on more complex geometries, and improved modelling of boundary conditions. Adaptive mesh refinement will be employed to tune the local numerical resolution to the needs of geometry representation.

Acknowledgements The authors gratefully acknowledge support by the Deutsche Forschungsgemeinschaft (DFG) as part of collaborative research center SFB 1029 “Substantial efficiency increase in gas turbines through direct use of coupled unsteady combustion and flow dynamics” on project C01. M.N. and R.K. thank Phillip Blakeley and Nikos Nikiforakis (Cavendish Labs., Cambridge University) for very productive cooperation on code development.

References

1. Berger, M.J., Colella, P.: Local adaptive mesh refinement for shock hydrodynamics. *J. Comput. Phys.* **82**, 67–84 (1989)
2. Berger, M.J., Helzel, C.: A simplified h-box method for embedded boundary grids. *SIAM J. Sci. Comput.* **34**(2), A861–A888 (2012)
3. Colella, P., Graves, D.T., Keen, B.J., Modiano, D.: A Cartesian grid embedded boundary method for hyperbolic conservation laws. *J. Comput. Phys.* **211**(1), 347–366 (2006)
4. Fritsch, F.N., Carlson, R.E.: Monotone piecewise cubic interpolation. *SIAM J. Numer. Anal.* **17**(2), 238–246 (1980)
5. Günther, Claudia, Meinke, Matthias, Schröder, Wolfgang: A flexible level-set approach for tracking multiple interacting interfaces in embedded boundary methods. *Comput. Fluids* **102**, 182–202 (2014)
6. Gray, J.A.T., Lemke, M., Reiss, J., Paschereit, C.O., Sesterhenn, J., Moeck, J.P.: A compact shock-focusing geometry for detonation initiation: experiments and adjoint-based variational data assimilation. *Combust. Flame* **183**, 144–156 (2017)
7. Hu, X.Y., Khoo, B.C., Adams, N.A., Huang, F.L.: A conservative interface method for compressible flows. *J. Comput. Phys.* **219**, 553–578 (2006)

8. Klein, R., Bates, K.R., Nikiforakis, N.: Well-balanced compressible cut-cell simulation of atmospheric flow. *Philos. Trans. R. Soc. Lond. A Math. Phys. Eng. Sci.* **367**(1907), 4559–4575 (2009)
9. Meinke, M., Schneiders, L., Günther, C., Schröder, W.: A cut-cell method for sharp moving boundaries in Cartesian grids. *Comput. Fluids* **85**, 135–142 (2013)
10. Skews, B.W.: The shape of a diffracting shock wave. *J. Fluid Mech.* **29**(2), 297–304 (1967)
11. Strang, G.: On the construction and comparison of difference schemes. *SIAM J. Num. Anal.* **5**, 506–517 (1968)
12. Toro, E.F.: *Riemann Solvers and Numerical Methods for Fluid Dynamics: A Practical Introduction*. Springer, Heidelberg (2009)
13. van Leer, Bram: On the relation between the upwind-differencing schemes of Godunov, Engquist-Osher and Roe. *SIAM J. Sci. Stat. Comput.* **5**(1), 1–20 (1984)
14. Willert, C.E., Mitchell, D.M., Soria, J.: An assessment of high-power light-emitting diodes for high frame rate Schlieren imaging. *Exp. Fluids* **53**(2), 413–421 (2012)